Monthly Notices
of the
ROYAL ASTRONOMICAL SOCIETY

MNRAS **440,** 150–160 (2014)
Advance Access publication 2014 March 7

doi:10.1093/mnras/stu185

A panchromatic analysis of starburst galaxy M82: probing the dust properties

Susan Hutton, Ignacio Ferreras,* Kinwah Wu, Paul Kuin, Alice Breeveld, Vladimir Yershov, Mark Cropper and Mat Page

Mullard Space Science Laboratory, University College London, Holmbury St Mary, Dorking, Surrey RH5 6NT, UK

Accepted 2014 January 24. Received 2014 January 20; in original form 2013 July 5

ABSTRACT

We combine near-ultraviolet (NUV), optical and IR imaging of the nearby starburst galaxy M82 to explore the properties of the dust both in the interstellar medium of the galaxy and the dust entrained in the superwind. The three NUV filters of *Swift*-Ultraviolet/Optical Telescope enable us to probe in detail the properties of the extinction curve in the region around the 2175 Å bump. The NUV colour–colour diagram strongly rules out a 'bump-less' Calzetti-type law, which can either reflect intrinsic changes in the dust properties or in the star formation history compared to starbursts well represented by such an attenuation law. We emphasize that it is mainly in the NUV region where a standard Milky Way-type law is preferred over the Calzetti law. The age and dust distribution of the stellar populations is consistent with the scenario of an encounter with M81 in the recent $\lesssim$400 Myr. The radial variation of NUV/optical/IR photometry in the galaxy region – including the polycyclic-aromatic-hydrocarbon-dominated emission at 8 μm – confirms the central location of the star formation. The radial gradients of the NUV and optical colours in the superwind region supports the hypothesis that the emission in the wind cone is driven by scattering from dust grains entrained in the ejecta. The observed wavelength dependence, $\propto\lambda^{-1.5}$, reveals either a grain size distribution $n(a) \propto a^{-2.5}$, or a flatter distribution with a maximum size cutoff, suggesting that only small grains are entrained in the supernova-driven wind.

Key words: dust, extinction – galaxies: evolution – galaxies: individual: NGC 3034 – galaxies: starburst – galaxies: stellar content.

1 INTRODUCTION

Nearby star-forming galaxies provide the opportunity to probe our knowledge of the mechanisms controlling star formation. Located at a distance of 3.5 Mpc (Dalcanton et al. 2009), and with a dynamical mass of $\sim 10^{10}$ $M_\odot$ (Greco, Martini & Thompson 2012), M82 (NGC 3034) is the closest starburst galaxy, and its edge-on orientation reveals a prominent outflow powered by the accumulated energy injection from supernovae into the interstellar medium (ISM; see, e.g. Mac Low & Ferrara 1999). Lynds & Sandage (1963) argued that M82 underwent an 'explosion' leading to the expulsion of gas along the minor axis. The strong star formation sustained by this galaxy is believed to have been triggered by a close encounter with the more massive galaxy M81, located in the same group. Dynamical modelling of the system suggests this encounter took place between 300 Myr (Yun, Ho & Lo 1993) and 1 Gyr ago (Sofue 1998), and there is a prominent distribution of gas and dust in the intergalactic region between them (Yun et al. 1993; Roussel et al. 2010).

Multiband photometry reveals a young population overall with a luminosity-weighted age between 100 and 450 Myr, and a central (inside 500 pc) region dominated by younger (∼10 Myr) stars (Mayya, Carrasco & Luna 2005; Mayya et al. 2006; Rodríguez-Merino, Rosa-González & Mayya 2011), possibly formed over a number of episodic bursts lasting a few million years each (Förster Schreiber et al. 2003). Detailed observations of star clusters in the central region and throughout the disc support this view (Smith et al. 2006; Konstantopoulos et al. 2009; Westmoquette et al. 2009). Furthermore, recent hydrodynamical simulations suggest that many massive stellar clusters must have formed over the past 10 Myr in order to explain the multiphase properties of the wind (Melioli, de Gouveia Dal Pino & Geraissate 2013). Further out in the disc, the central starburst may have also caused a decrease of the star formation rate, as revealed by the low number of red supergiants (Davidge 2008).

The UV/optical/IR emission in the wind region extends out to ∼10 kpc (Devine & Bally 1999; Lehnert, Heckman & Weaver 1999). The polarization of the Hα emission (e.g. Visvanathan

* E-mail: i.ferreras@ucl.ac.uk

& Sandage 1972; Yoshida, Kawabata & Ohyama 2011) is explained by scattering from dust particles entrained in the superwind (Sanders & Balamore 1971). *GALEX* UV imaging of the wind region confirms that neither shock-heated nor photoionized gas can be the dominant mechanisms of emission (Hoopes et al. 2005). The positive detection of polycyclic aromatic hydrocarbons (PAH) in the infrared with *Spitzer* (Engelbracht et al. 2006) and *AKARI* (Kaneda et al. 2010), and an even more extended distribution of cool dust seen by *Herschel* (Roussel et al. 2010), give further support to this scenario, although additional processes in the superwind have to be considered when dealing with the emission lines (McKeith et al. 1995). Ohyama et al. (2002) split the wind region into a diffuse component – responsible for the scattered light – and a filamentary component, explained by shocks around the hot gas. In addition to a supernova-driven mechanism, Roussel et al. (2010) suggest that over two-thirds of the dust in the intergalactic region could have been removed from the M81/M82 system via tidal interactions.

In this paper, we take advantage of the increased spectral resolution around the 2175 Å bump, provided by the *Swift*/UVOT passbands, in order to probe the dust properties in M82. In addition to exploring the stellar populations in the galaxy, we extend the analysis to the wind region by analysing the wavelength dependence of the light scattered away from the galactic disc. The structure of the paper is as follows: the NUV-to-IR data used for the analysis are presented in Section 2, followed by the photometric analysis with population synthesis and dust attenuation models in Section 3. In Section 4, we present a simple model to constrain the properties of the dust entrained in the supernova-driven wind. Finally, our conclusions are given in Section 5.

2 DATA

The near-ultraviolet (NUV) science-grade images of M82 were retrieved from the *Swift* archive at HEASARC.[1] The Ultraviolet/Optical Telescope (UVOT; Roming et al. 2005) is one of three telescopes on board the *Swift* spacecraft (Gehrels et al. 2004). For our purposes of targeting the dust properties of M82, UVOT has an optimal set of three broad-band filters in the NUV, straddling the 2175 Å bump (Poole et al. 2008). The camera covers a field of view of 17 × 17 arcmin^2; hence, a single pointing covers the M82 and superwind region, mapping a 18 × 18 kpc^2 area at the distance of M82. The resolution of the telescope is between 2.4 and 2.9 arcsec (FWHM) in the NUV filters (Breeveld et al. 2010a). The observational data for this paper were taken between 2008 and 2012 (see Table 1 for details). The total exposure time amounts to 10.21, 13.95 and 8.70 ks in the *UVW*2, *UVM*2 and *UVW*1 passbands, respectively. All images were aspect corrected. In addition, the standard corrections for large-scale sensitivity (Breeveld et al. 2011) and the slow drift in zero-point (Breeveld et al. 2010b) were applied. The individual exposures were registered and co-added using a standard drizzle algorithm (Fruchter & Hook 2002), with a 0.5 arcsec pixel size. Each ObsID set comprises several frames, so in total we have around 50 frames in each band. Drizzling enables us to improve the S/N ratio and the spatial resolution of the co-added image. Throughout this paper we compute magnitudes within the standard 5 arcsec (radius) aperture. We note this aperture is accurately calibrated (Poole et al. 2008; Breeveld et al. 2010a) and minimizes the contribution from the tails of the point spread function (PSF). Table 2 summarizes the details of the passbands used in this paper, along with the 3σ limiting aperture magnitudes. These magnitudes were obtained by taking 1000 measurements within the same-sized circular apertures, in blank outer regions of the images, away from the galaxy or other contaminating sources. The distribution of the aperture magnitudes is shown in Fig. 1 both for the galaxy and the wind footprint. Note that the UVOT data are deep, so that the photometry in the galaxy and wind regions is at least 2 mag brighter than the 3σ limit. Hence, the statistical uncertainty of the photometric measurements remains below the 5 per cent level. The combined effect of zero-point uncertainties (3 per cent; Breeveld et al. 2011) and correction for Galactic foreground dust (see below) results in a total uncertainty of 0.1 mag. Regarding the Milky Way foreground correction, we take the revised value of reddening from the NED data base towards M82 ($E(B-V) = 0.140$ Gyr), based on the recalibration (Schlafly & Finkbeiner 2011) of the Schegel, Finkbeiner & Davis (1998) dust maps. Along with the tabulated colour excess, we ran a large set of synthetic population models from Bruzual & Charlot (2003) to compute the effect of the stellar

[1] http://heasarc.gsfc.nasa.gov/docs/swift/

Table 1. Log of *Swift*/UVOT observations of NGC 3034 used in this paper.

ObsID	Date	Exposure time (s) *UVW*2 2033 Å	*UVM*2 2229 Å	*UVW*1 2591 Å
00031201001	2008/05/01	1660.68	1660.67	1469.57
00031201002	2009/04/25	–	4636.08	–
00032503003	2012/07/06	–	973.11	–
00032503004	2012/07/13	954.40	–	–
00032503006	2012/07/27	–	–	1042.70
00035482001	2007/01/26	1518.53	999.43	758.71
00035482002	2009/10/18	1442.39	1038.59	719.94
00091489001	2012/04/05	413.15	413.15	428.54
00091489002	2012/04/06	1572.38	1572.53	1260.46
00091489003	2012/04/08	1256.48	1256.47	1424.05
00091489004	2012/04/10	289.15	289.15	263.69
00091489005	2012/04/14	111.98	111.98	130.21
00091489006	2012/04/15	875.34	875.41	1038.83
00091489007	2012/04/17	118.87	118.86	159.45
	TOTAL	10 213.35	13 945.43	8696.15

Table 2. Properties of the passbands and limiting magnitudes.

Filter	⟨λ⟩ (Å)	FWHM (Å)	Apert. limit 3 σ(AB)	MW corr[a] (mag)
		UVOT		
*UVW*2	2033	657	24.39	1.07
*UVM*2	2229	498	24.28	1.17
*UVW*1	2591	693	23.77	0.88
		GALEX		
FUV	1539	230	23.00	1.26
NUV	2316	793	23.96	1.27
		SDSS		
SDSS*u*	3551	599	20.70	0.67
SDSS*g*	4686	1379	22.17	0.52
SDSS*r*	6165	1382	21.59	0.36
SDSS*i*	7481	1535	20.62	0.27
SDSS*z*	8931	1370	20.44	0.20
		Other		
Hα	6573	67	16.80	0.36
IRAC/ch4	79 274	28 427	16.65	0.01

[a] Foreground Galactic attenuation correction towards M82 (see Section 2 for details).

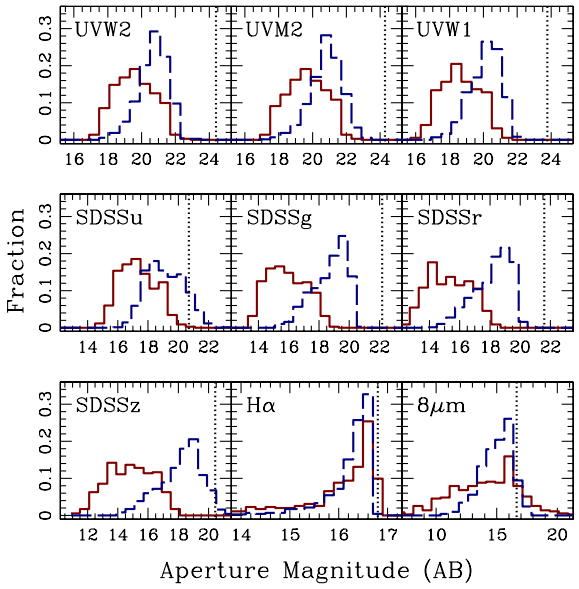

Figure 1. Distribution of aperture magnitudes in the galaxy (solid red histograms) and the wind region (blue dashed). In each panel, we also include the limiting magnitude derived from the distribution of fluxes measured in 1000 random apertures in the background (vertical dotted line). Note the histograms of the *GALEX*/FUV and SDSS-*i* photometry are not included in this figure to avoid overcrowding, see Table 2 for information about these bands.

population properties on the correction for the different passbands. We use a wide range of ages and metallicities, applying the standard $R_v = 3.1$ Milky Way attenuation law (Fitzpatrick 1999). The de-reddening correction (quoted in Table 2) is defined as the median value of the distribution for this range of models. We derive a systematic uncertainty from foreground de-reddening of 6 per cent in the UVOT UV filters (in contrast with the SDSS data, see below, where the correction introduces an error <1 per cent).

In addition to the NUV data, we retrieved optical images in the *u*, *g*, *r*, *i* and *z* bands from the DR8 version of the Sloan Digital Sky Survey (SDSS; Aihara et al. 2011). In order to bring the spatial resolution of the SDSS images (PSF FWHM $\lesssim$ 1.5 arcsec) in line with the UVOT data, we extracted an isolated stellar image from the UVOT *UVW2* frame, and used a rescaled version of this PSF frame as a convolution kernel for the SDSS images. The scale factor is chosen so that the PSF of the convolved images matches the one corresponding to the NUV data. Finally, the SDSS convolved frames were rescaled and registered to match the UVOT images. By comparing photometric measurements before and after this process, we estimate an additional 5–10 per cent error in the optical fluxes. The SDSS data are deep enough for our purposes, except for the wind region in the shallower *u*-band frame (see Fig. 1). Nevertheless, even in this case, only 11 per cent of the measurements fall below this limit, all of them at a projected galactocentric distance $R > 2.6$ kpc.

We retrieved and processed the Hα-subtracted image of M82 from the fifth data release of the Spitzer Infrared Nearby Galaxies Survey (SINGS; Kennicutt et al. 2003). The image, taken at the 2.1 m Kitt Peak National Observatory (KPNO) telescope, was processed the same way as the SDSS frames, to match the pixel size and resolution of the UVOT images. In addition, we made use of the *Spitzer* Infrared Array Camera (IRAC) 8 μm image of M82, also retrieved from the SINGS data release. Given the resolution of this image, we decided only to register and rescale the 8 μm data to the reference frame. Finally, the *GALEX* images were retrieved from the Atlas of Nearby Galaxies (Gil de Paz et al. 2007). In this paper, we use only the FUV data, because the NUV photometry is comparable to UVOT/*UVM2* (see, e.g. Page et al. 2012).

Fig. 2 (*left*) shows a colour composite of our data, with the blue, green and red channels of the RGB image corresponding to *UVW2*, SDSS *g* and Hα, respectively. Note the significant colour difference between the bulk of the galaxy – mostly blue-green, implying that it is dominated by intermediate stellar ages – and the central region, showing intense Hα and UV emission from young, massive stars. In the outer regions, perpendicular to the plane of the disc, the dominant emission is in the UV, reflecting the contribution from dust scattering (see Section 4).

From these images we derived a photometric catalogue, separately for the galaxy and the superwind region, by selecting a number of 5 arcsec (radius) apertures, as shown on the right-hand panel of Fig. 2. We took care in removing apertures in the areas contaminated by foreground/background sources. This is especially

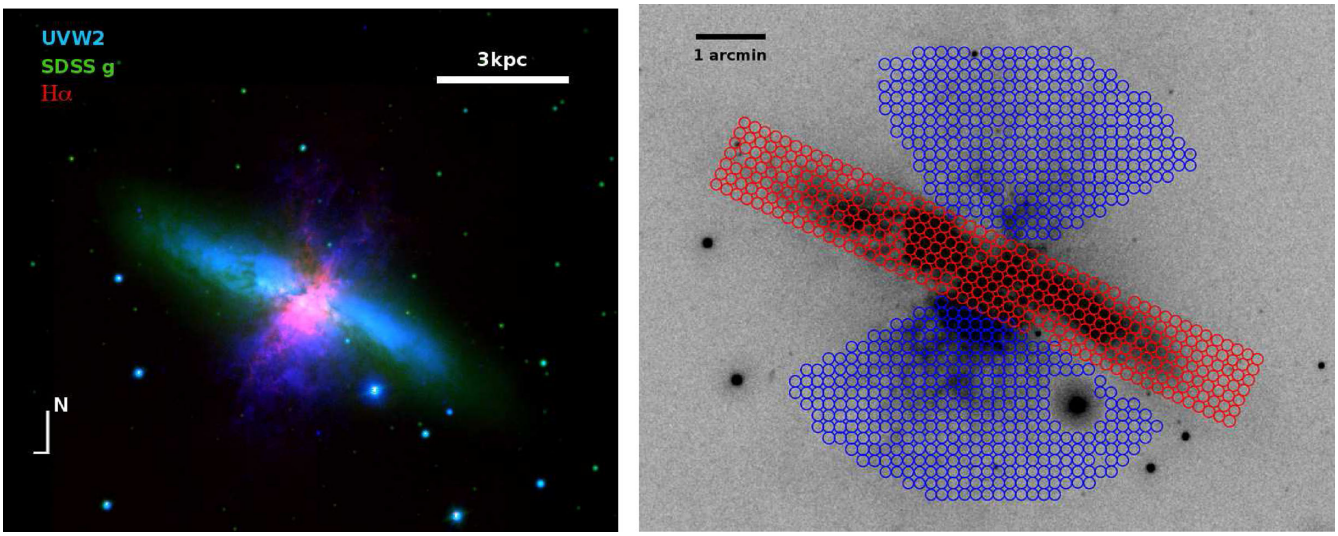

Figure 2. *Left:* RGB colour composite of M82 using UVOT/*UVW2* (blue), SDSS/*g* (green) and narrow band Hα (red). Note the wide extent of the NUV light in the wind region. *Right:* apertures used for the analysis of the galaxy (red) and the wind region (blue). Each aperture has a radius of 5 arcsec. The grey-scale background image is that from the *UVW2* filter.

important in the wind region, where bright sources would introduce a number of outliers in the study of the photometry. The final data set uses 351 (695) apertures in the galaxy (wind) footprint.

3 PHOTOMETRY OF THE GALAXY REGION

Given the passband response curves of the UVOT NUV filters (see, e.g. Breeveld et al. 2011), a colour–colour diagram using these filters is a powerful discriminant of the dust extinction spectral properties of nearby galaxies, especially in the region around the 2175 Å bump. Although the origin of the bump is not clear, it matches a resonance in transitions involving C-ring structures such as graphite, or PAH compounds (see, e.g. Duley & Seahra 1998). Even though this bump is strong in sightlines probing the ISM of the Milky Way galaxy (Fitzpatrick & Massa 1986), it seems to be absent in starburst galaxies (Calzetti 2001). The lack of a strong bump could be indicative of changes in the dust properties (Gordon, Calzetti & Witt 1997). However, an age-dependent attenuation law from an otherwise identical dust component can also give rise to different bump strengths (Panuzzo et al. 2007).

3.1 NUV photometry and dust extinction

Fig. 3 shows an NUV colour–colour diagram with the three UVOT filters. All four panels show the same photometric data, and each panel overlays a different set of models. Each red line tracks an age sequence corresponding to a simple stellar population (SSP) from the models of Bruzual & Charlot (2003), at either solar metallicity ($Z_\odot$, *top*) or $Z_\odot/10$ (*bottom*). The lines span a wide range of ages, from 0.1 to 10 Gyr (all models run with age increasing from left to right). Within each panel, the different lines probe a range of reddening values, from a colour excess of $E(B-V)=0$ (in the top of each panel) to 1 mag, in steps of 0.25 mag. Since these models only explore the evolution of a synthetic stellar population, these tracks should be compared with the photometry in the galaxy region (grey points). However, for reference, we also show the photometric data in the wind region (blue crosses). Finally, the models are also divided with respect to the extinction law, using the Calzetti (2001) prescription in the left-hand panels, and a Milky Way extinction law (Fitzpatrick 1999) on the right-hand panels.

Note that although the models span a wide range of age, metallicity and colour excess, the Calzetti extinction law (*left*) cannot account for the observations. The Fitzpatrick (1999) law, however, covers all the data points, suggesting that the extinction law of a starburst galaxy such as M82 shows a prominent NUV bump. The *UVW*2−*UVM*2 and *UVM*2−*UVW*1 colours straddle the 2175 Å bump, so this diagram is especially constraining with respect to the presence of the bump. We show below that using models with composite stellar populations still yields the same rejection of the Calzetti extinction law in M82. Note the increasingly blue value of the *UVW*2−*UVM*2 colour with increasing age. This is caused by the presence of a red leak that introduces flux in the *UVW*2 filter for older populations. We emphasize that the models take into account the red leak.

Even though the models cannot be compared with the photometric data in the wind (blue crosses), this figure illustrates the significantly bluer colours in this region. The photometry in the wind region reveals the presence of dust entrained in the gas ejected from a supernova -driven wind (Hoopes et al. 2005). This dust scatters light from the central starburst. A detailed photometric analysis allows us to constrain the properties of the dust (the next section).

In Fig. 4, we extend the colour–colour diagrams to optical wavelengths. The data points show the photometry from only the galaxy region, splitting the sample with respect to the projected radial

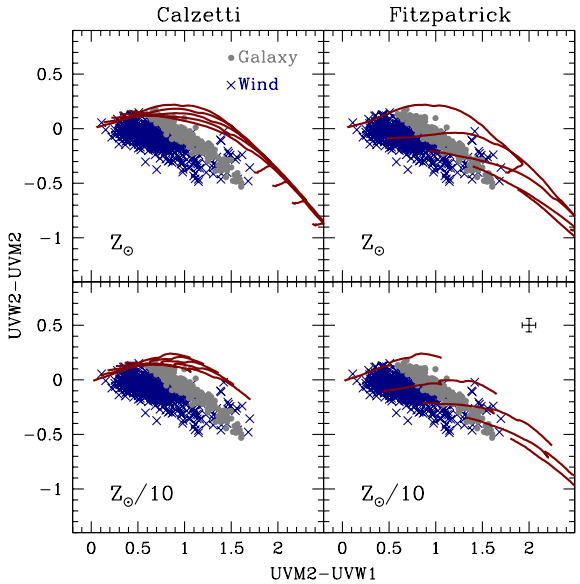

Figure 3. NUV colour–colour plots for the galaxy (grey filled circles) and wind (blue crosses) regions, within a projected galactocentric distance of 3 kpc. This figure compares the model predictions for two different extinction laws: Calzetti (2001; *left*) and Fitzpatrick (1999; *right*). Each line represents an age sequence from 0.1 to 10 Gyr for an SSP from Bruzual & Charlot (2003) at solar metallicity (*top*) and $Z_\odot/10$ (*bottom*). The lines in each panel corresponds to different values of the colour excess arising from the extinction, from top to bottom, $E(B-V)=\{0, 0.25, 0.50, 0.75, 1\}$ mag. A characteristic 1σ error bar is shown in the bottom-right panel.

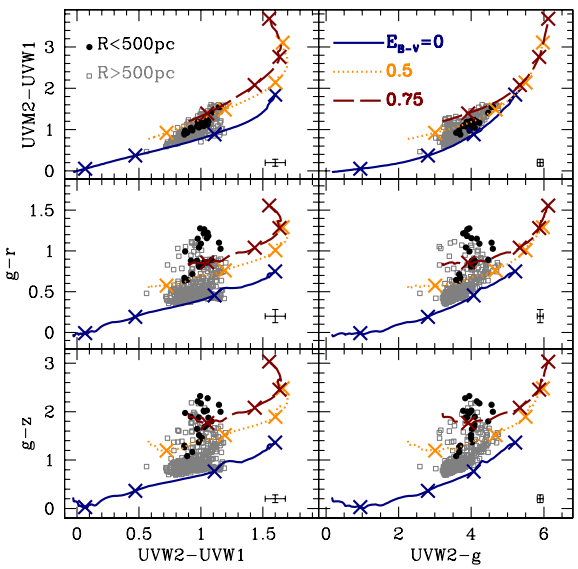

Figure 4. NUV and optical colour–colour diagrams of the photometric data in the galaxy region. The sample is split with respect to the projected galactocentric distance (R), as labelled. For reference, an age sequence at solar metallicity is shown, from the models of Bruzual & Charlot (2003) assuming a dustless population (blue solid lines) and two dusty cases (orange dotted lines for $E(B-V)=0.5$; and red dashed lines for $E(B-V)=0.75$), following the Fitzpatrick (1999) extinction law. The crosses mark, from left to right, stellar ages of 0.1, 0.5, 1 and 5 Gyr. A typical error bar is shown in each panel.

Table 3. Model parameters used for the grid of star formation histories. Each model is defined by the star formation rate, $\psi(t)$. In the EXP models, we define t_U as the age of the Universe at $z = 0$.

Observable	Parameter	Range	Steps
Single Burst (SSP): $\psi(t) \propto \delta(t - t_0)$			
Age	$\log(t_0/\mathrm{Gyr})$	-2 to $+0.7$	64
Metallicity	$\log Z/Z_\odot$	-2 to $+0.3$	16
Dust	$E(B-V)$	0–1	32
		Number of models	32 768
Two bursts (2SSP): $\psi(t) \propto [f_Y \delta(t - t_Y) + (1 - f_Y)\delta(t - t_O)]$			
Age, old	(t_O/Gyr)	$0.5 - 12$	16
Age, young	$\log(t_Y/\mathrm{Gyr})$	-2 to -0.3	16
Young mass fraction	f_Y	0–1	16
Metallicity	$\log Z/Z_\odot$	-2 to $+0.3$	16
Dust	$E_{(B-V)}$	0–1	32
		Number of models	2097 152
Exponentially decaying rate (EXP): $\psi(t) \propto \exp[-(t - t_{FOR})/\tau]$			
Formation time	$\log t_S \equiv \log[(t_U - t_{FOR})/\mathrm{Gyr}]$	-1 to $+1$	32
Time-scale	$\log(\tau/\mathrm{Gyr})$	-1 to $+1$	32
Metallicity	$\log Z/Z_\odot$	-2 to $+0.3$	16
Dust	$E(B-V)$	0–1	32
		Number of models	524 288
		TOTAL	2.65×10^6

distance between the core – where the starburst is taking place (black dots, $R < 500$ pc) – and the rest of the galaxy (grey dots). We overlay in each panel three tracks showing SSPs at solar metallicity, with ages ranging from 30 Myr (bottom left of each panel) to 5 Gyr. Crosses mark the ages of 0.1, 0.5, 1 and 5 Gyr, for reference. The blue solid lines follow a dustless model, whereas the orange dotted (red dashed) lines introduce a 0.5 mag (0.75 mag) colour excess according to the favoured Fitzpatrick (1999) extinction law.

3.2 Modelling the stellar populations

We present here an extended analysis of the stellar populations, exploring a wide range of star formation histories to derive a more quantitative assessment of the extinction law. We run three grids of models corresponding to different star formation histories: single burst models (SSP); two-burst models (2SSP) and exponentially decaying models (EXP). Table 3 shows the model parameters and the sampling used in the grids. We use the population synthesis models of Bruzual & Charlot (2003) to build the grids. In addition to the parameters controlling the age distribution and the metallicity, we include an additional parameter that describes the amount of reddening, via a colour excess, $E(B - V)$, following either the extinction law of Fitzpatrick (1999) or Calzetti (2001). For each aperture, we define a χ^2 in the usual manner, by comparing model (MOD) and measured (OBS) data, using the SDSS g-band measurement as normalization. Specifically, for each aperture, we define

$$\chi^2 \equiv \sum_{i=1}^{8} \frac{\left(c_i^{\mathrm{MOD}} - c_i^{\mathrm{OBS}}\right)^2}{\sigma^2\left(c_i^{\mathrm{OBS}}\right)}, \quad (1)$$

where the $\{c_i\}$ represent the aperture colours, defined as

$$c_i = \begin{cases} g - X_i, & i < 8 \\ \mathrm{FUV} - UVW2_c, & i = 8 \end{cases}$$

with $X_i = \{UVW2, UVM2, UVW1, u, r, i, z\}$ ($i < 8$), and $\sigma(c_i^{\mathrm{OBS}})$ is the uncertainty of the ith observed colour. The last term ($i = 8$) corresponds to the colour between the *GALEX* FUV band and *UVW2*, where the comparison requires the *UVW2* image to be convolved to the (lower) resolution of the FUV passband, thus the notation $UVW2_c$. Fig. 5 (*left*) shows the probability-weighted age (*top*) and colour excess (*bottom*), for the Fitzpatrick (1999) extinction law, corresponding to the single burst (SSP) models. For reference, the age and dust reddening estimates from Rodríguez-Merino et al. (2011) are included as grey shaded regions, showing good agreement within the uncertainties. We note that metallicity is treated in this paper as a nuisance parameter: although metallicity cannot be constrained with this type of photometric data alone, we need to explore a range of values of metallicity in order to extract robust estimates of the age and dust content. The distribution of reduced χ^2_r values has a median of 0.70, and ∼90 per cent of the data points have $\chi^2_r < 3.0$. Hence, the reduced values of χ^2 stay around $\chi^2_r \sim 1$–3, showing that the fits are quite acceptable. Fig. 6 illustrates the goodness of fit with three typical cases at different galactocentric radii (as labelled). The error bars indicate the aperture photometry (the horizontal error bars span the full width at half-maximum (FWHM) of the filter). The blue line corresponds to the best-fitting spectrum in each case. The same apertures are shown for the Fitzpatrick (*left*) or the Calzetti (*right*) extinction law. Note the significant mismatch of the NUV photometry when using the Calzetti function, revealing the presence of the NUV bump.

Fig. 5 (*right*) shows the parameters of the best fits for the composite population models: the top panels give the fraction in young mass stars (f_Y) with respect to the age of the young component (t_Y), whereas the bottom panels show the exponential time-scale (τ) and the average stellar age for the EXP models. In both cases, we split the sample into two panels (*left*/*right*), with respect to the projected galactocentric distance, as labelled. Note that in the outer region, the populations are well described by a relatively homogeneous population with ages in the range 0.5–1.5 Gyr, regardless of the model used.

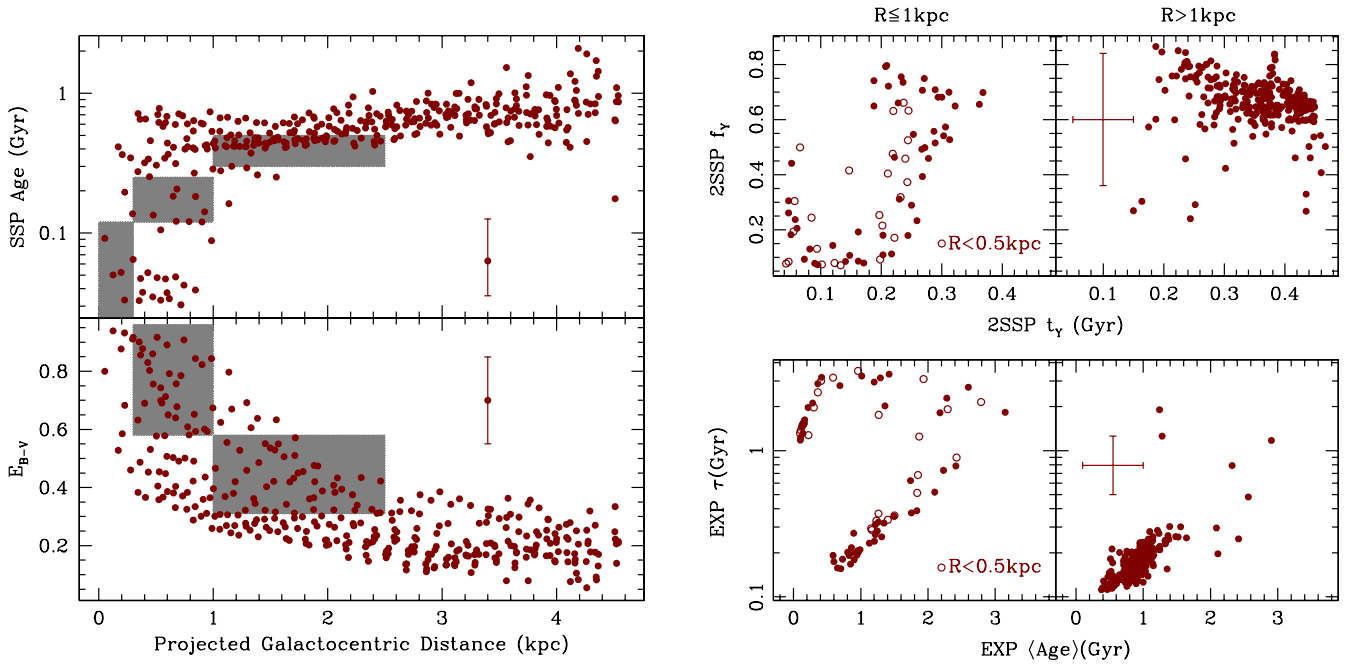

Figure 5. *Left*: best-fitting SSP equivalent ages (*top*) and colour excess (*bottom*) of the data in the galaxy region, obtained by a comparison with a set of 32 768 SSPs from the models of Bruzual & Charlot (2003) (see the text for details). A characteristic 1σ error bar is shown in each case. The grey regions correspond to the range of ages and colour excess from Rodríguez-Merino et al. (2011). *Right*: best fits for composite models: the top panels show the values of the young component in age (t_Y) and stellar mass fraction (f_Y) for the 2SSP models, whereas the bottom panels correspond to the average age and time-scale for the exponentially decaying SFHs. The data are split with respect to galactocentric distance, as labelled (top), and typical 1σ error bars are included in the rightmost panels.

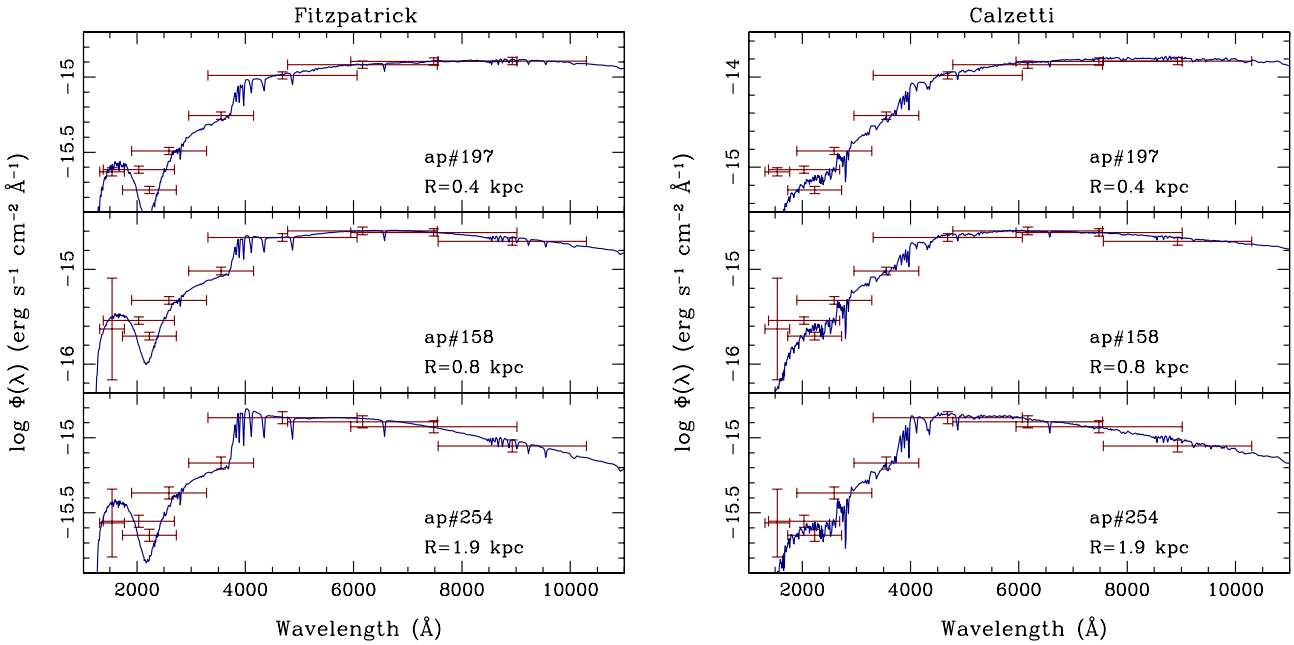

Figure 6. Comparison between observed NUV/optical photometry (red error bars) and the best-fitting models (blue) for three aperture measurements at different galactocentric distances, as labelled. The best fits are shown assuming either the Fitzpatrick (*left*) or the Calzetti (*right*) dust extinction law. Note the significant difference between these two in the NUV region, where the bump creates a dip in the Fitzpatrick case.

Within the central kpc, the populations are significantly younger, although the modelling is unable to distinguish whether the younger ages are caused by an extended period of star formation (i.e. EXP models) or after a recent burst (i.e. 2SSP models). For the general sample, the distribution $\Delta\chi^2 \equiv \chi^2_{\rm min,2SSP} - \chi^2_{\rm min,EXP}$ has a mean of -1.3 with an rms of 2.9, i.e. slightly favouring a two-burst scenario.

Fig. 7 provides a more quantitative confirmation of the preference of a Milky Way (hereafter MW) type of extinction law with respect

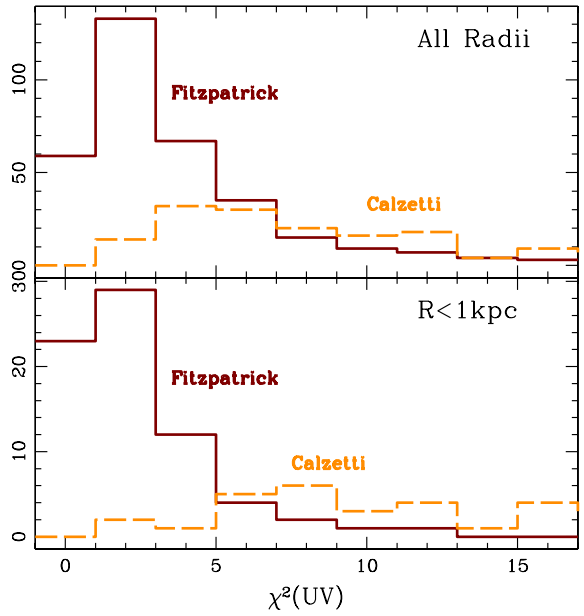

Figure 7. Comparison of the best fits between the Calzetti (dashed lines) and the Fitzpatrick (solid lines) extinction law. Both optical and NUV photometry is used to constrain the model parameters (as in Fig. 5), but in this case we use the NUV photometry to define a new statistic, $\chi^2(UV)$. The results are restricted to models with an acceptable *total* reduced $\chi^2_r < 5$ for either the Calzetti, or the Fitzpatrick model), and with a corresponding colour excess of $E_{(B-V)} \gtrsim 0.1$ mag. The distributions for the inner regions ($R < 1$ kpc) are shown in the bottom panel. A wide range of star formation histories are explored, including SSPs; exponentially decaying models and a two-burst superposition (see text for details).

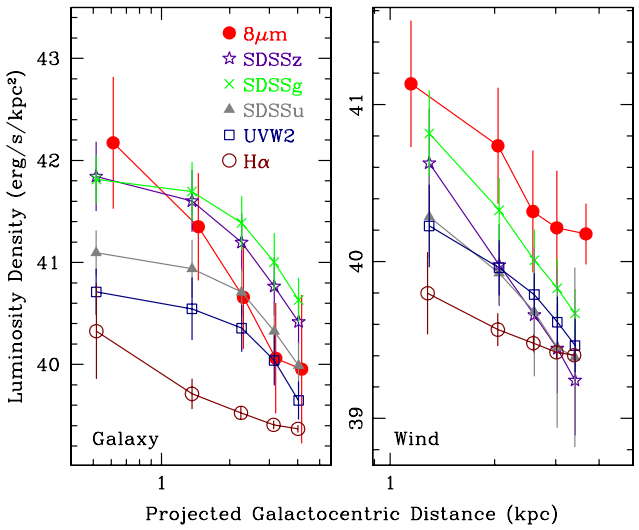

Figure 8. Radial profile of luminosity density in the galaxy (*left*) and wind region (*right*) of M82. The points correspond to the median value within bins in projected radial position (the binning is done at fixed number of data points per bin). The rms scatter in each bin is shown as an error bar.

to a 'bump-less' Calzetti (2001) extinction curve. It compares the χ^2 of the respective models, restricting the results to NUV photometry (i.e. only using the information from FUV, *UVW*2, *UVM*2 and *UVW*1 to define the statistic). For a meaningful comparison, we consider only models that are acceptable, rejecting those results with a total reduced $\chi^2_r > 5$ in *either* the Calzetti or the Fitzpatrick cases. Only models with a best-fitting reddening $E(B-V) > 0.1$ mag are included, since regions with low reddening will not be sufficiently informative for the discrimination between extinction laws. In order to determine whether there are differences between the dust extinction law in the central starburst or the periphery – where a more standard MW-type behaviour is expected – the figure is split between the central kpc (in projection) and the outer regions. No significant changes are found, with an overall preference towards the Fitzpatrick extinction. One could expect that a projected measurement of an edge-on galaxy such as M82 would introduce an MW-type extinction from the outer regions seen along the line of sight. However, the fact that the ages and colour excess at $R < 1$ kpc are clearly different from the rest would imply that the central burst makes a large contribution to the photometry in many of the $R < 1$ kpc apertures. Therefore, we can tentatively conclude that the Calzetti law is not favoured in the starburst region of M82.

Fig. 8 compares the radial profile in the galaxy and wind regions at different wavelengths, from *UVW*2 to 8 μm, including Hα. There is a very sharp decrease of the 8 μm data in the galaxy region, in contrast with a milder gradient in the wind region, reflecting an additional contribution at 8 μm from intrinsic emission of the dust entrained in the wind material. In addition, the gradient at shorter wavelengths is shallower in the wind region, a consequence of the wavelength-dependent scattering of light from the dust component. This effect is easier to visualize in Fig. 9 (*left*), where we show the average value of the flux in several regions in the galaxy (*top*) and the wind (*bottom*). For reference, we include the integrated spectral energy distribution of M82 from the templates of Lonsdale et al. (2004). Note the good agreement in the central part of the galaxy, where the starburst phase is taking place. As we move further out along the galaxy disc, the PAH-dominated emission at 8 μm drops sharply. In contrast, the wind region shows a smaller decrease of the 8 μm flux with radial distance, and the NUV–optical spectrum becomes significantly bluer. In the next section, we will relate this trend with the properties of the dust entrained in the wind.

The comparison of the NUV/optical and FIR spectrum of M82 in Fig. 9 (*left*) raises the issue of the energetic balance between the light 'removed' by dust from the NUV/optical region, and the FIR emission – which corresponds to energy re-radiated by the heated dust. In other words, could M82 hide a heavily dust-enshrouded starburst whose FIR emission is unaccounted for in the NUV/optical window? Fig. 9 (*right*) shows the result for a simple model, where the original template of M82, shown in the leftmost panels, is de-reddened according to the colour excess, $E(B-V)$, which is taken as a free parameter (horizontal axis). The vertical axis represents the ratio between the observed total IR luminosity (measured at $\lambda > 8$ μm) and the *excess* luminosity in the UV and optical spectral region. The latter is obtained by subtracting the observed energy in the UV–optical range ($0.1 < \lambda/\mu m < 1$) from the one corresponding to the de-reddened spectrum for a given $E(B-V)$, using the standard Fitzpatrick (solid line) or Calzetti (dashed line) extinction law. Note that the $L_{IR}/\Delta L_{UV/Opt} = 1$ case (horizontal dotted line) corresponds to the 1:1 balance between the UV/optical light absorbed by dust and the dust emission at longer wavelengths. The histograms (*bottom*) are the distributions of best-fitting $E(B-V)$ obtained in the modelling of the stellar populations of the $R < 1$ kpc apertures (see, e.g. Fig. 5), confirming that the reddening thus obtained is consistent. Therefore, within uncertainties, all dust-enshrouded light is accounted for.

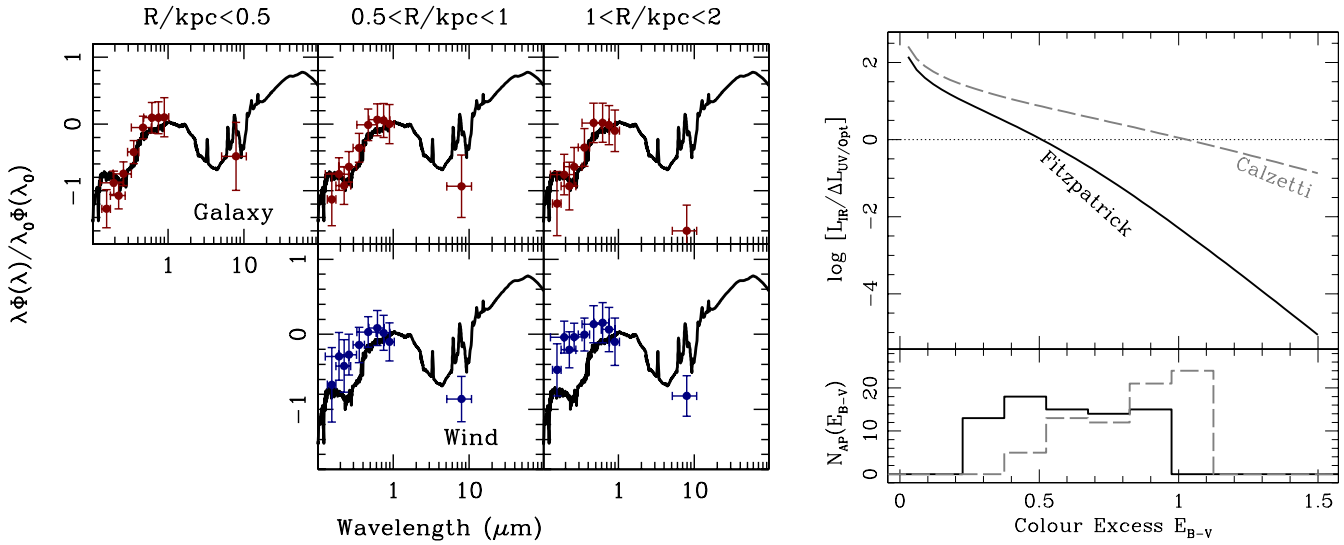

Figure 9. *Left*: comparison of the UV to IR spectral energy distribution in the galaxy (red points; top) and wind (blue points; bottom) regions, with respect to projected radial distance to the centre. The data include *GALEX*/FUV; UVOT/*UVW*2, *UVM*2, *UVW*1; SDSS/*u*, *g*, *r*, *i*, *z* and IRAC 8 μm. The horizontal error bars indicate the spectral coverage of each passband, while the vertical error bars show the rms scatter within each radial bin. The black line is a template of the M82 spectrum (Lonsdale et al. 2004). All data are normalized to the flux at $\lambda_0 = 0.8$ μm. Note the sharp decrease at 8 μm in the galaxy with increasing distance. In the wind region, the bluer SED is caused by starlight scattered from dust entrained in the wind, and the milder decrease in 8 μm reveals intrinsic emission far from the galactic plane. *Right*: (top) the ratio between the observed IR luminosity ($\lambda > 8$ μm) and UV/optical excess luminosity (estimated between the observed and the unreddened spectra in $0.1 < \lambda/\mu\mathrm{m} < 1$) is shown with respect to colour excess for the Fitzpatrick (black solid line) or Calzetti (grey dashed line) attenuation laws. Bottom: the histograms represent the best-fitting values from the SSP models for the $R < 1$ kpc apertures (see Fig. 5).

4 DUST IN THE SUPERWIND

4.1 Probing the dust properties

Fig. 10 shows the *UVW*2−*X* radial colour profiles in the wind region (blue crosses along with the rms scatter as error bars), with *X* ranging from *GALEX*/FUV to the SDSS *z* band, as labelled. For reference, the flatter radial profiles of the colours in the galaxy region are shown in each panel as a red line with a shaded area extending over the observed rms scatter. The colour gradients in the galaxy increase slightly with wavelength, as expected from typical variations in stellar age, metallicity and dust reddening. However, the gradients in the wind region are significantly steeper. Extrapolations of the colour in the wind region at galactocentric distances of 0 and 3 kpc are shown as star symbols. Light from the wind region can be explained only by scattering, shocks or photoionization. However, the recent analysis of Hoopes et al. (2005), using *GALEX* UV and Hα photometry reject the last two, leaving dust scattering as the main cause for the observed light.

In this section, we explore the constraints one can enforce on the distribution of dust via the wavelength dependent change between the light in the central part of the galaxy – where the emission originates – and the outer region of the wind – where the contribution is almost exclusively caused by dust scattering. We determine the change induced by scattering from the colour change between the measurements at projected galactocentric distances of $R = 0$ and 3 kpc. As a reference, the error bars on the left-hand side of each panel in Fig. 10 give the predicted colours of a model for all measurements at $R < 1$ kpc, for which the dust screen from the best-fitting result is removed, keeping the age and metallicity unchanged. The large scatter is a result of the wide range of values of $E(B-V)$ in the central region of the galaxy (see Fig. 5, *left*). These colours are in most cases bluer than the photometric measurements

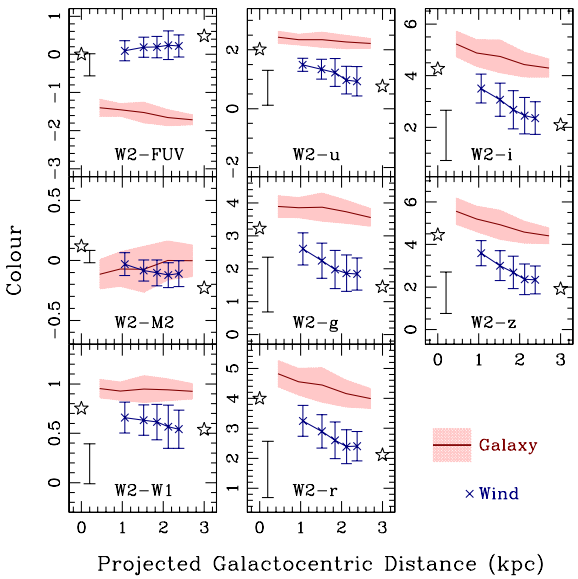

Figure 10. Radial plots of the measured colours in the wind (blue crosses) and galaxy areas (red line and shaded regions). The colours, *UVW*2−*X*, with *X* ranging from *UVM*2 to SDSS-*z*, are given as the median values, binned at a fixed number of data points per bin. The error bars and the extent of the shaded regions give the rms spread within each bin. The stars show the extrapolated colours in the wind region at $R = 0$ and 3 kpc. The error bar on the left-hand side of each panel is the predicted best-fitting SSP models at $R < 1$ kpc when the dust screen is removed (see the text for details).

in the wind, showing that the illumination source from the starburst must be significantly affected by dust. The variation of the colours between $R = 0$ and 3 kpc in the wind region are shown with respect to wavelength in Fig. 11 (filled dots), where the error bars

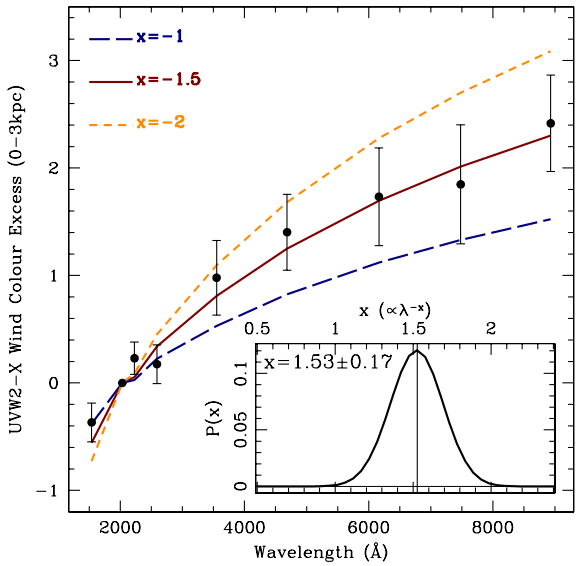

Figure 11. Colour variation between the galaxy and the wind against wavelength. The black filled circles are the observations, including the rms scatter as error bars. The three lines correspond to different dust scattering laws, proportional to λ^{-x}. The inset shows the probability distribution function for the power-law index x.

correspond to the rms scatter. For reference, a generic dust scattering law is assumed:

$$\sigma_{\rm scat} \propto \lambda^{-x}. \quad (2)$$

The three lines in the figure represent the expectation for three choices of x, as labelled. Assuming the incident light originates in the central starburst, we use SSP models with the same age and reddening properties as in the central regions of the galaxy (see Fig. 5), and modify the spectrum according to equation (2). The inset gives the probability distribution function keeping x as a free parameter, where we find $x = 1.53 \pm 0.17$ (1σ error bar). We note that in the limit of small particle size (Rayleigh scattering), $x = 4$, whereas in the opposite regime of dust grains much larger than the incident wavelength, $x = 0$ is expected (see, e.g. Draine 2011).

4.2 A simple dust scattering model

The radiation from the galactic wind cone of M82 is probably scattered light from the starburst in the central region by free electrons, molecules and dust entrenched in the wind outflows. Scattering by free electrons is practically Thomson scattering, whose cross-section is independent of the wavelength of the incident radiation. Scattering by molecules can be described as the Rayleigh scattering process – given the smaller size of the molecules with respect to the wavelength of the optical/NUV radiation. The cross-section of Rayleigh scattering scales as λ^{-4}, thus the process preferably scatters the higher frequency radiation away from the incident rays. Scattering by dust particles is more complicated. However, as an approximation, if we neglect the thermodynamics of the process, we may employ the Mie prescription, in which the scattering dust kernels are modelled by dielectric or metallic spheres and the incident radiation as waves. There are two distinctive regimes in this scattering process, depending on the ratio between the wavelength of the incident radiation and the size of the scattering spheres. The critical wavelength (λ_c) that divides the two regimes is therefore determined by the characteristic size of the scattering sphere (a_c). Radiation with $\lambda > \lambda_c$, will be scattered with the Rayleigh scaling. For $\lambda < \lambda_c$ – if ignoring resonant features, the cross-section is practically independent of the wavelength of the incident radiation, and the process will be described by Thomson scattering. Note that these different regimes have distinguishable angular dependence. However, because of the specific geometrical setting of the source and the orientation of the wind cone in M82, the angular dependence of the scattering processes does not play a very significant role in determining the wavelength dependence of the observed radiation in the weak scattering limit.

We now show that the observed $\propto\lambda^{-1.53}$ dependence of the radiation in the NUV/optical data can be explained by a simple dust scattering model. We assume an incident radiation originating from a point source in the core of the galaxy. The observed light in the wind region results from the scattering of this radiation by the dust particles in the wind cone. We consider spherical dust particles with some distribution of sizes. Even though the particle density can vary with location, we enforce the same distribution of dust grain size everywhere in the wind cone. As the sizes of the dust particles relative to the wavelengths of the incident radiation determine whether the scattering is in the Rayleigh regime or in the Thomson regime, the scattering optical depth is wavelength dependent. One can define a critical wavelength λ_c that reflects the transition from one regime to the other. If all dust grains had the same size, we would expect a trivial spectral break in the wavelength dependence of the scattered light at λ_c – see panel (a) of Fig. 12, where $\lambda_c = 2000$ Å is assumed. An ensemble of dust particles with different sizes smears the spectral break into a broad region, depending on the particle size distribution.

In the weak scattering approximation, the intensity scattered into the line of sight $I_{\rm sc}$ from the incident rays, with intensity I_0, may be expressed as

$$I_{\rm sc}(\lambda) \approx \tau_{\rm sc}(\lambda)\ \left(I_0(\lambda)\,{\rm e}^{-\tau_{\rm ex}(\lambda)}\right)\Big|_r, \quad (3)$$

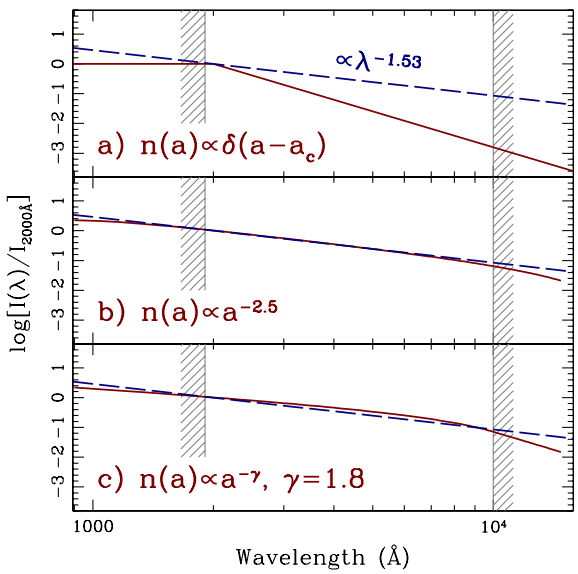

Figure 12. Predictions for the intensity of light scattered by the three simple dust models considered in Section 4 (see the text for details). The grey shaded regions mark the ends of the observed wavelength coverage, and the blue dashed line in all three panels corresponds to a fiducial $\propto\lambda^{-1.53}$ behaviour, from the observational constraints (see Fig. 11).

where τ_{sc} is the scattering optical depth and τ_{ex} is the extinction depth evaluated at the projected location $\boldsymbol{r}$. This expression takes into account the attenuation of the incident radiation due to scattering and absorption when propagating through the scattering wind cone. In the spectral calculation, the optical depths $\tau_{sc}(\lambda)$ and $\tau_{ex}(\lambda)$ can be derived using a parametric prescription with the weights of the critical wavelength λ_c determined by the convolution of the grain size distribution. We can therefore compute the spectrum of the scattered radiation using a reference incident spectrum, such as the SED of the star-forming region in the core of M82 (red circles in Fig. 9, left-hand panel, at $R < 1$ kpc).

In panel (b) of Fig. 12, we show that the observed $\propto\lambda^{-1.53}$ dependence (Fig. 11) can be obtained by a dust model for the wind cone with a size distribution $n(a) \propto a^{-2.5}$, where a is the dust grain radius. In addition, the particles must have upper and lower size limits such that the critical wavelengths corresponding to these size limits fall outside of the wavelength range covered (i.e. limited by the grey shaded regions in Fig. 12). An almost perfect power law is obtained, with similar wavelength dependence to our results. Alternatively, the grain size distribution can be flatter, i.e. $n(a) \propto a^{-\gamma}$, where the power-law index $\gamma < 2.5$, with an additional constraint on the maximum size of the dust particles. The critical wavelengths corresponding to the largest grains must lie within the wavelength range covered by the observations. In this case, we would not obtain a power law but the result would be compatible with the observed $\propto\lambda^{-1.53}$ behaviour. This dependence is due to the presence of a broad transition region between the Rayleigh scattering regime (with λ^{-4} dependence) and the Thomson scattering regime (practically independent of λ) within the spectral range covered. Panel (c) of Fig. 12 demonstrates that an acceptable fit can be generated for a dust size distribution $n(a) \propto a^{-1.8}$ with the additional constraint of an upper size limit (a_{MAX}), that gives a critical wavelength $\lambda_c(a_{MAX}) \simeq 1$ μm.

5 CONCLUSIONS

M82 is the nearest starburst galaxy, allowing us to explore with a high level of detail the various processes of this important phase of galaxy evolution. We present here a study of deep NUV images taken by the UVOT on board the *Swift* observatory. We combine them with additional UV, optical and IR archival data, to explore the properties of the stellar populations in the galaxy, and the dust entrained in the supernova-driven wind. The NUV colour–colour diagram – especially sensitive to the presence of the 2175 Å bump – reveals a strong rejection of traditional extinction curves used for starburst galaxies (Calzetti 2001) which lack a bump. The standard MW extinction (e.g. Fitzpatrick 1999) is favoured (Fig. 3). The stellar populations reveal a very young core, with luminosity-weighted ages $\lesssim$100 Myr and large extinction ($E(B-V) \gtrsim 0.5$ mag) at projected galactocentric distances $R < 1$ kpc. In the outer regions, the galaxy has an overall homogeneous distribution of 0.7–1 Gyr old populations, with lower, but significant ($E(B-V) \sim 0.2$ mag) colour excess (Fig. 5). In the wind region, the spectral energy distribution is bluer, and the PAH-dominated emission at 8 μm does not decrease with galactocentric distance as sharply as along the disc (Fig. 8). These two trends reflect the contribution from dust scattering, and from intrinsic dust emission, respectively. In addition, the energy balance between the observed IR ($\lambda > 8$ μm) emission and the UV/optical ($\lambda < 1$ μm) energy absorbed by dust according to our best-fitting models, suggests that there is no excess energy in the form of a heavily dust-enshrouded starburst (see Fig. 9, *right*).

By comparing the colours in the wind region over a wide separation in galactocentric distance, $\Delta R = 3$ kpc, we quantify the wavelength-dependent scattering. We obtain a behaviour $\propto\lambda^{-1.5}$ (Fig. 11), implying either a distribution of dust grain sizes as $n(a) \propto a^{-2.5}$, or a flatter distribution, e.g. $n(a) \propto a^{-1.8}$, along with an upper size limit that results in a critical wavelength within the spectral coverage of the instrumentation. Although detailed values of this size limit would require information about the grain composition, this result would suggest that only small grains are entrained in the supernova-driven wind.

ACKNOWLEDGEMENTS

This research has made use of data and web tools obtained from NASA's High Energy Astrophysics Science Archive Research Center (HEASARC), a service of Goddard Space Flight Center and the Smithsonian Astrophysical Observatory. We have made use of data from the Sloan Digital Sky Survey (SDSS). An extended acknowledgement to the excellent SDSS archive can be found at the following link: http://www.sdss.org/collaboration/credits.html.

REFERENCES

Aihara H. et al., 2011, ApJS, 193, 29
Breeveld A. A. et al., 2010a, MNRAS, 406, 1687
Breeveld A. A. et al., 2010b, Swift-UVOT, CALDB-15-02b
Breeveld A. A., Landsman W., Holland S. T., Roming P., Kuin N. P. M., Page M. J., 2011, in McEnery J. E., Racusin J. L., Gehrels N., eds, AIP Conf. Proc. Vol. 1358, Gamma Ray Bursts 2010. Am. Inst. Phys., New York, p. 373
Bruzual G., Charlot S., 2003, MNRAS, 344, 1000
Calzetti D., 2001, New Astron., 45, 601
Dalcanton J. J. et al., 2009, ApJS, 183, 67
Davidge T. J., 2008, AJ, 136, 2502
Devine D., Bally J., 1999, ApJ, 510, 197
Draine B., 2011, Physics of the Interstellar and Intergalactic Medium. Princeton Univ. Press, Princeton, NJ
Duley W. W., Seahra S., 1998, ApJ, 507, 874
Engelbracht C. W. et al., 2006, ApJ, 642, L127
Fitzpatrick E. L., 1999, PASP, 111, 63
Fitzpatrick E. L., Massa D., 1986, ApJ, 307, 286
Förster Schreiber N. M., Genzel R., Lutz D., Sternberg A., 2003, ApJ, 599, 193
Fruchter A. S., Hook R. N., 2002, PASP, 114, 144
Gehrels N. et al., 2004, ApJ, 611, 1005
Gil de Paz A. et al., 2007, ApJS, 173, 185
Gordon K. D., Calzetti D., Witt A. N., 1997, ApJ, 487, 625
Greco J. P., Martini P., Thompson T. A., 2012, ApJ, 757, 24
Hoopes C. G. et al., 2005, ApJ, 619, L99
Kaneda H. et al., 2010, A&A, 514, A14
Kennicutt R. C. et al., 2003, PASP, 115, 928
Konstantopoulos I. S., Bastian N., Smith L. J., Westmoquette M. S., Trancho G., Gallagher J. S., 2009, ApJ, 701, 1015
Lehnert M. D., Heckman T. M., Weaver K. A., 1999, ApJ, 523, 575
Lonsdale C. et al., 2004, ApJS, 154, 54
Lynds C. R., Sandage A. R., 1963, ApJ, 137, 1005
McKeith C. D., Greve A., Downes D., Prada F., 1995, A&A, 293, 703
Mac Low M.-M., Ferrara A., 1999, ApJ, 513, 142
Mayya Y. D., Carrasco L., Luna A., 2005, ApJ, 628, L33
Mayya Y. D., Bressan A., Carrasco L., Hernández-Martínez L., 2006, ApJ, 649, 172
Melioli C., de Gouveia Dal Pino E. M., Geraissate F. G., 2013, MNRAS, 430, 3235
Ohyama Y. et al., 2002, PASJ, 54, 891
Page M. J. et al., 2012, MNRAS, 426, 903
Panuzzo P., Granato G. L., Buat V., Inoue A. K., Silva L., Iglesias-Páramo J., Bressan A., 2007, MNRAS, 375, 640
Poole T. S. et al., 2008, MNRAS, 383, 627

Rodríguez-Merino L. H., Rosa-González D., Mayya Y. D., 2011, ApJ, 726, 51
Roming P. W. A. et al., 2005, Space Sci. Rev., 120, 95
Roussel H. et al., 2010, A&A, 518, L66
Sanders R. H., Balamore D. S., 1971, ApJ, 166, 7
Schegel D. J., Finkbeiner D. P., Davis M., 1998, ApJS, 500, 525
Schlafly E. F., Finkbeiner D. P., 2011, ApJ, 737, 103
Smith L. J., Westmoquette M. S., Gallagher J. S., O'Connell R. W., Rosario D. J., de Grijs R., 2006, MNRAS, 370, 513
Sofue Y., 1998, PASJ, 50, 227
Visvanathan N., Sandage A., 1972, ApJ, 176, 57
Westmoquette M. S., Gallagher J. S., Smith L. J., Trancho G., Bastian N., Konstantopoulos I. S., 2009, ApJ, 706, 1571
Yoshida M., Kawabata K. S., Ohyama Y., 2011, PASJ, 63, 493
Yun M. S., Ho P. T. P., Lo K. Y., 1993, ApJ, 411, L17

This paper has been typeset from a TEX/LATEX file prepared by the author.